

Observation and Wiener filtering of oceanic microseisms with mixed wave content

M Coughlin,¹ J Harms,^{2,3} P Meyers,⁴ D.C. Bowden,⁵
V Mandic,⁴ G Pavlis,⁶ T Prestegard,⁴ and V.C. Tsai⁵

*¹Division of Physics, Math, and Astronomy,
California Institute of Technology, Pasadena, CA 91125, USA*

²Gran Sasso Science Institute (GSSI), I-67100 LAquila, Italy

³INFN, Laboratori Nazionali del Gran Sasso, I-67100 Assergi, Italy

*⁴School of Physics and Astronomy, University of Minnesota,
Minneapolis, Minnesota 55455, USA*

⁵Seismological Laboratory, California Institute of Technology, Pasadena, CA 91125, USA

*⁶Department of Geological Sciences,
Indiana University, Bloomington, IN 47405, USA*

Abstract

The Sanford Underground Research Facility in the former Homestake mine in South Dakota and surrounding land contained an array of 24 seismometers studying the properties of the underground seismic environment. One use of the array is to study the benefit of constructing an underground gravitational-wave detector in the quiet seismic environment. Due to predicted sensitivity limitations at low frequency from terrestrial gravity noise, commonly known as Newtonian noise, it is important to study the potential for coherent Newtonian-noise subtraction using seismometers. In previous work, we used Wiener-filtering techniques to subtract coherent noise in a smaller seismic array in the frequency band $0.05 - 1$ Hz, achieving more than an order of magnitude noise cancellation over a majority of this band. In this paper, we demonstrate significant improvement over these results being able to use a larger number of seismometers as input to the Wiener filter. The increased extent of the array allows us to investigate correlations between seismometers in greater detail, which is required to define more accurate Newtonian-noise models and to predict the performance of Newtonian-noise cancellation systems for underground detectors. Specifically, we found evidence that body waves dominate oceanic microseisms at 0.2 Hz during times when the spectral density approaches the global low-noise model being perturbed by typically week-long fundamental Rayleigh-wave transients. Such mixed wave fields would pose a substantial additional challenge to the cancellation of seismic Newtonian noise in ground-based, sub-Hz, gravitational-wave detectors.

PACS numbers: 95.75.-z, 04.30.-w

I. INTRODUCTION

With the recent detections of gravitational waves from binary black holes [1–4] and binary neutron stars [5], interest in the development of new technology for sensitivity improvements as upgrades of the existing gravitational-wave detectors or for future-generation detectors is being renewed. The network of advanced gravitational-wave detectors consists of the two Advanced LIGO interferometers in the United States [6], the Advanced Virgo interferometer in Italy [7], GEO-HF in Germany [8], the KAGRA interferometer in Japan [9], and the LIGO-India detector in India [10]. In the future, third-generation detectors, such as Cosmic Explorer [11] and the Einstein Telescope [12], will be an order of magnitude more sensitive than these.

Sophisticated seismic-isolation systems are used in order to limit the effect of seismic disturbances. The Advanced LIGO seismic isolation is a combination of active and passive isolation stages [13, 14], while the Advanced Virgo seismic isolation is a mostly passive system [15]. Additional suppression of seismic noise can be achieved with feed-forward cancellation [16–19]. In addition, fluctuations in the gravitational field at the test mass from local seismic noise and temperature and pressure fluctuations in the atmosphere, which are known as Newtonian noise (NN), will be a future limiting noise source below about 20 Hz [20–23]. For this reason, future gravitational-wave detectors are likely to be built at sites with low levels of ambient seismic noise [24, 25] or constructed underground [12]. Previously, the Homestake mine was identified as a world-class, low-noise environment [25–27]. Feed-forward techniques similar to those used for seismic disturbances can also be used to subtract NN [28, 29].

In previous work [26], we implemented feed-forward noise cancellation using an array of 3 seismometers located at the Sanford Underground Research Facility in the Black Hills of South Dakota [25]. We used Wiener filters, which are the optimal linear filters to cancel noise of (wide-sense) stationary random processes defined in terms of correlations between witness and target sensors [30, 31]. We explored how to maximize subtraction, including exploring the rate at which the filters are updated and the number of filter coefficients. There were limits to this original study. Due to the fact that we only had 3 functional seismometers, we could not explore the effect of body waves on the coherence between the seismometers and thus the subtraction that we could achieve. In addition to the self-noise of the seismometers, topographic scattering and body waves in the seismic field could limit

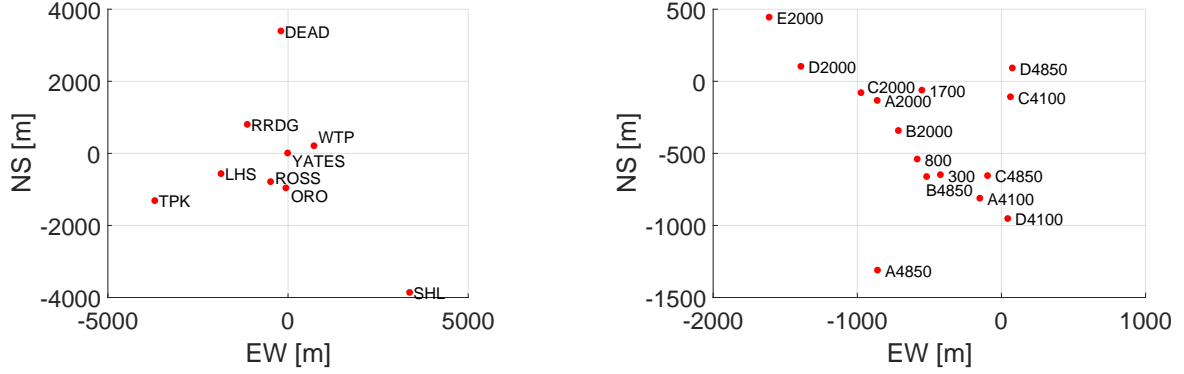


FIG. 1: Sketch of array configuration as function of horizontal coordinates. Left: surface stations, right: underground stations.

performance due to the filters only being able to subtract sources of noise that are always present [32].

Efforts have been made in the wider seismological community to understand and exploit this background ambient seismic noise. The strongest mechanism for the generation of seismic noise relates to continuous harmonic forcing of ocean waves as they interact with both the seafloor and coastlines, and this varies strongly in time, frequency and azimuth [33–37]. These mechanisms most strongly generate surface waves in the range of 8 to 16 second periods, but a much wider range of periods is also observed worldwide and there can also be strong body wave components as well [38]. Efforts to image these noise sources use array processing methods that consider the coherency of wavefronts incident upon the array, referred to as beamforming or f-k analysis [39–42], similar in many ways to the efforts here. Special attention has been paid to understanding the effect that the inhomogeneous distribution of noise sources would have on measured coherency or cross-correlation [43], with the goal of determining whether such measurements can be reliably used for the study of seismic velocities [44, 45] or attenuation [46, 47]. Wiener filtering is complementary to these techniques, which predominantly depend on the coherence between only two stations and subsequently stack observations or estimate parameters based on a model, and instead uses the coherence between all stations in the array when making predictions.

In the new seismic array, there are 24 seismometers, 15 underground and 9 above ground (see figure 1) [27]. These broadband instruments are sensitive to seismic noise between about 10 mHz and 50 Hz, which covers both the primary and secondary microseism appearing

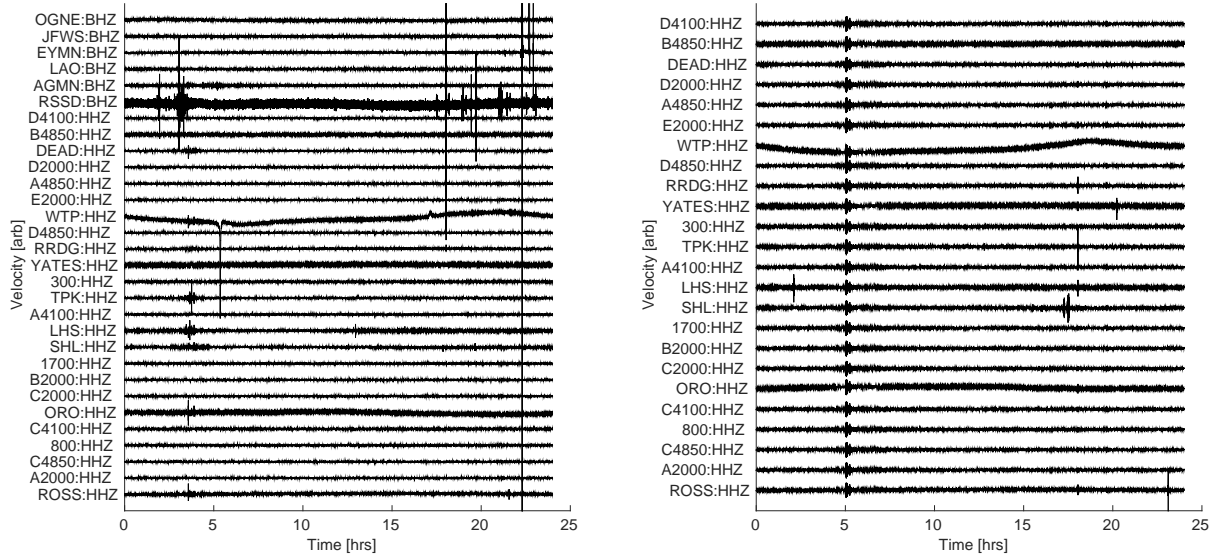


FIG. 2: Time series for the two days analyzed in section III. Left: time series on day 154 of year 2015, right: time series of day 191 of 2015. (Take out traces belonging to stations not shown in figure 1.)

between 30 – 100 mHz, and 0.1 – 0.5 Hz respectively, as well as the anthropogenic band between 1 Hz and a few tens of Hz. In this array, the horizontal distances between some of the seismometers cover more than 6000 m, which is about 5 times the extent of the original array, while the vertical distances extend about 1500 m. Time series of two days of data for the stations in the array are shown in figure 2.

In section II, we present measurements of seismic speeds. Correlation measurements between seismometer pairs are discussed in section III. In section IV, the Wiener filtering method is described, and results presented for the coherent cancellation of seismic noise in selected target seismometers. Our conclusions are summarized in section V.

II. SEISMIC SPEED MEASUREMENTS

Seismic speeds are not of primary interest for NN modeling, but they can be useful to interpret correlation measurements between sensors. Seismic correlations are of great importance to model NN and to design and predict the performance of noise-cancellation systems [23].

Assuming that seismic scattering can be neglected, and that all seismic sources are sufficiently distant, we can divide the seismic field into three components: plane shear waves, compressional waves, and surface Rayleigh and Love waves. Our goal is to obtain speed estimates by observing the ambient seismic field. In this case, an additional challenge (relative to methods using specific earthquake events) is that there can be multiple waves contributing simultaneously at all frequencies. The array dimension then sets a lower limit to the range of frequencies where multiple waves can be disentangled to obtain well-defined differential phases between sensors.

We use a correlation method to extract information from the ambient seismic field. The first step was to calculate the complex spectral coherence of all of the vertical channels of seismometer pairs using 1 hour of data. The 1-hour coherences between seismometers i, j were collected over several months in their complex form

$$\gamma_{ij}(f) = \frac{\langle x_i(f) x_j^*(f) \rangle}{\sqrt{\langle |x_i(f)|^2 \rangle \langle |x_j(f)|^2 \rangle}} \quad (1)$$

where $x_i(f)$ is the value of the Fourier Transform at a particular frequency f for the i th seismometer and $x_i^*(f)$ its complex conjugate. This metric keeps information about relative phases between seismometers. For the speed measurements, each coherence value was calculated using the Welch method with 128s FFT length and no overlap. The next step was to calculate the corresponding k-f map, which is a 3-dimensional data product with the two components of the horizontal wave-vector on two axes and frequency on the third. This can be understood as a parameterized stacking method, where a plane-wave model is used to search over all possible phase shifts as a function of propagation directions and seismic speed:

$$m(\vec{k}, f) = \sum_{i,j} \gamma_{ij}(f) e^{i\vec{k}(f) \cdot \vec{r}_{ij}}, \quad (2)$$

where \vec{r}_{ij} are the relative position vectors between seismometers, and the wave vector $\vec{k}(f)$ is determined by seismic speed and propagation direction. We make histograms of seismic speeds at each frequency bin proportional to $m(\vec{k}, f)$ and add them in order to construct probability distributions for the seismic speeds. In contrast to a simple stacking method, this method also takes into account the degree of coherence as contributions from low-coherence pairs are suppressed. If the dimensions of the array and seismometer spacing are favorable, then one can potentially find multiple distinct local maxima, which correspond to different,

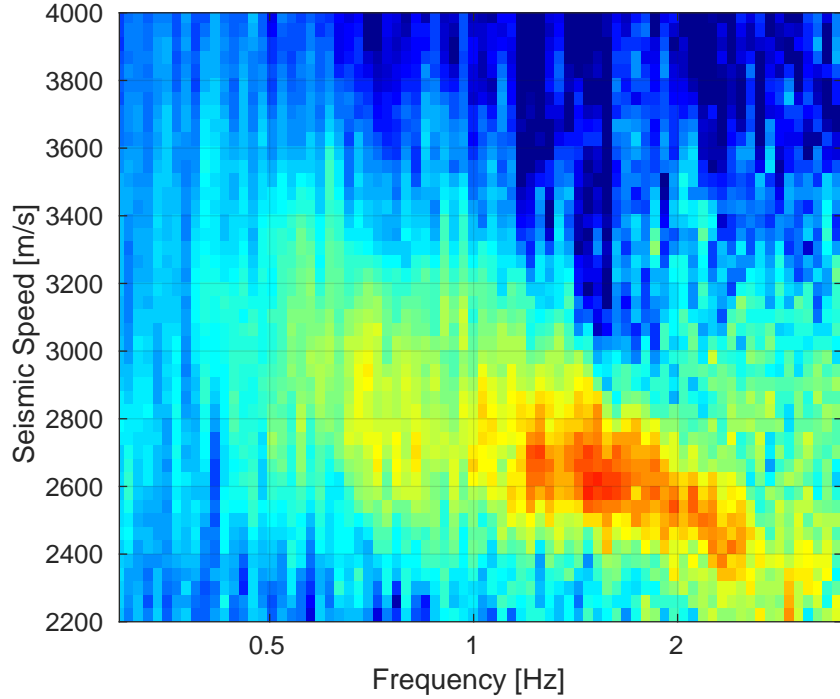


FIG. 3: The plot shows a histogram of seismic speeds between 0.3 – 3.5 Hz. Red color means that the respective speed value was measured for a large number of k-f maps, while blue color means that the speed value was measured rarely.

simultaneously present waves.

The k-f maps are calculated for each 1-day coherence matrix, and collected to produce histograms covering a period of about one year. One such histogram is shown in figure 3. The plot shows seismic speeds in the range between 0.3 Hz to 3.5 Hz. The distribution of maxima tends to lower speed values at higher frequencies, which is the normal dispersion of Rayleigh waves. We do not get meaningful speed estimates above 2.5 Hz since coherence between stations becomes very low above 2.5 Hz. At the same time, the array dimension prevented us from obtaining good estimates of seismic speeds below 1 Hz, where the width of the histogram is too large to clearly identify a specific mode. It was possible to decrease the width of the distribution by increasing correlation time, but 1-day averaging was about the maximum that could be done keeping a sufficiently high number of samples for the histogram. The histogram traces out a dispersion curve consistent in shape and absolute value with Rayleigh-wave models.

III. CORRELATION MEASUREMENTS

Understanding a seismic field in terms of its two-point spatial correlations, i.e., estimated from correlations between two seismometers, is fundamental to the understanding of NN and its cancellation [23]. Let us start by taking a look at the complex coherence $\gamma(f)$ defined in equation (1) between seismometers of the Homestake array. Here, in contrast to the speed measurements, coherence was calculated with 50% overlap, and in this form also used later for the Wiener filter.

The left plot in figure 4 shows the difference $1 - |\gamma(f)|$. Accordingly, coherence is generally high within the band of the primary and secondary oceanic microseismic peaks between a few tens of mHz and 1 Hz, and is insignificant above a few Hertz. Distances (horizontal distances) between the seismometers are (from top to bottom of legend): 250 m (200 m), 1600 m (900 m), 1400 m (1400 m), 1500 m (900 m), 1500 m (1500 m), 1600 m (650 m). At most frequencies, the shorter the horizontal distance, the higher the coherence.

The right plot shows the logarithm of $1 - |\gamma(f)|$ at 0.2 Hz for day 191 of year 2015 in a scatter plot where the two coordinates are the components of the relative horizontal position vector between two seismometers. We do not include a third coordinate for depth since Rayleigh waves, which are the dominant contribution at these frequencies on day 191 (see below), are known to produce displacement whose phase does not depend on depth. Coherence is well characterized by the horizontal distance between seismometers. There are no major inhomogeneities, but close inspection of the plot reveals significant directional dependence approximately aligned with the north-northwest-south-southeast and west-southwest-east-northeast directions.

We investigate coherence further by plotting it explicitly as a function of distance. The result is shown in figure 5 at 0.2 Hz for the two days 154 and 191 of year 2015, where we have plotted the real part $\Re(\gamma)$ of the complex coherence (RPCC) for the vertical channels. The plots show a bimodal distribution, which is a consequence of the directional dependence of the seismic field together with the directional non-uniformity of the seismic array. The directional dependence of the seismic field is expected from the known distribution of sources of oceanic microseisms observed at Homestake [25].

We can also exclude any significant impact from local sources at 0.2 Hz irrespective of whether they produce coherent or incoherent disturbances between stations. Observations

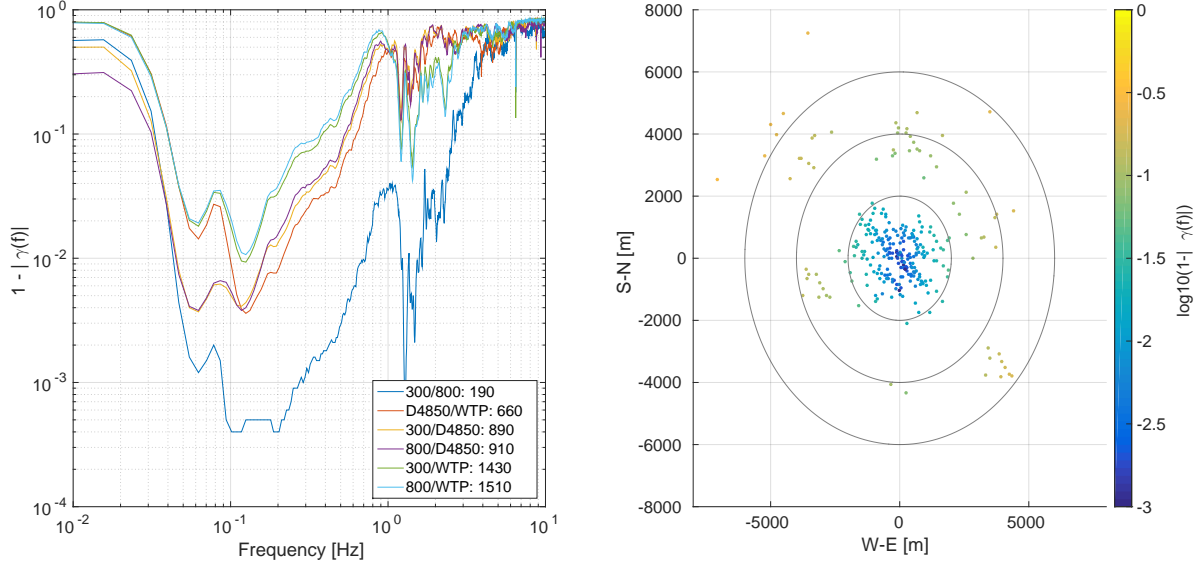


FIG. 4: Left plot: $1 - |\gamma(f)|$ between a variety of seismometer pairs averaged over 6 months of coincident data divided into 128s segments. The legend indicates the horizontal distance in meters between each pair shown, and the pairs are shown in ascending order of horizontal distance. Right plot: logarithm of $1 - |\gamma(f)|$ at 0.2 Hz between all seismometers, where the x,y-coordinates correspond to the relative horizontal position vector between two seismometers.

covering the entire area of the US showed that speeds of fundamental Rayleigh waves at 25s period are about 3.6 km/s [48]. Together with our results in figure 3, we can infer that Rayleigh-wave speed at 0.2 Hz should have a value around 3 km/s, which means that the lengths of all types of waves is larger than the array dimension. We also checked that coherence does not decrease systematically when increasing correlation time from one day to a month or longer, which means that there are no significant incoherent disturbances either that would average out over long periods of time. Next, we know from our observation of seismic spectra that local disturbances must be weaker than oceanic microseisms by a factor 10 or more since there is no disturbance visible even when oceanic microseisms are close to their minimum. Finally, if local sources had such a big effect on correlations, then they would have an equally significant effect on our Wiener filters (see following sections). However, this can be excluded since the Wiener filters prove to be highly efficient with the cancellation of oceanic microseisms (reduction by more than two orders of magnitude in most cases), which is only possible if the filter is almost fully determined by correlations

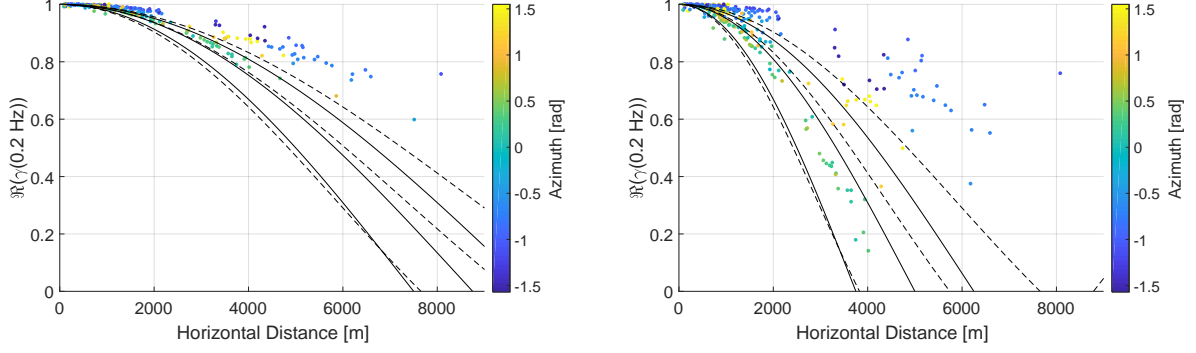


FIG. 5: The RPCC as a function of distance between the vertical channels of all seismometers at 0.2 Hz (left: day 154; right: day 191). The colors correspond to the azimuth with respect to the east direction of the line connecting two seismometers. On the left, models are shown for the single plane wave (solid lines; speed values 6 km/s, 7 km/s, 8 km/s), and isotropic field (dashed lines; speed values 4 km/s, 5 km/s, 6 km/s). The same models were used in the right plot with speed values 3 km/s, 4 km/s, 5 km/s (solid lines; single plane wave), and 2 km/s, 3 km/s, 4 km/s (dashed lines; isotropic).

consistent with oceanic microseisms.

Directional dependence of the seismic field only explains a variation of coherence values at fixed distance as a function of azimuth; it does not, however, explain the bimodal distribution. The latter can be explained by the directional non-uniformity of the seismic array. Almost all of the pairs in figure 5 with horizontal distance > 2 km include a surface station since surface stations are generally located at a greater distance from the main underground array. Surface stations TPK, WTP, and LHS lie on a line pointing approximately along the E-W direction, while the line DEAD, SHL is almost perpendicular to it (see figure 1). Identifying seismometer pairs of the > 2 km coherence values, we find that SHL and DEAD appear in the high-coherence part while TPK, LHS, and WTP appear in the low-coherence part. This is consistent with a directional dependence of a seismic field consisting mainly of waves propagating along the E-W direction, and the bimodal structure is enforced by the approximate cross-shape of the surface array.

An important parameter for the design of NN cancellation systems is the distance at which $\Re(\gamma) = 0.5$. For an isotropic Rayleigh-wave field, this value is observed at a distance r of about $\lambda/4$ (determined by a Bessel correlation function $J_0(2\pi r/\lambda)$), where λ is the length

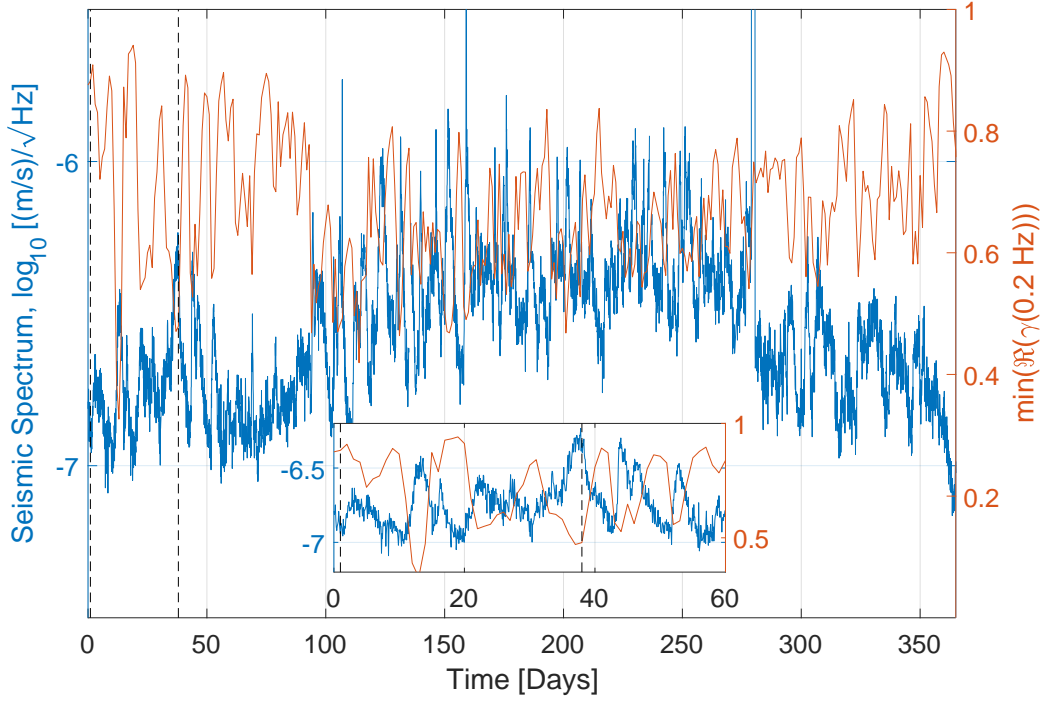


FIG. 6: The plot shows the power spectral density (PSD) of the 800 ft station at 0.2 Hz and the minimum coherence among all station pairs whose distance is less than 3 km where the dashed vertical lines mark the two days used for the coherence plots corresponding to days 154 and 191 of year 2015.

of Rayleigh waves. Instead, assuming maximal directional dependence from a single plane Rayleigh wave propagating in the direction of the separation line between two seismometers, the distance between the seismometers needs to be $\lambda/6$ to observe $\Re(\gamma) = 0.5$ (according to a cosine correlation function $\cos(2\pi r/\lambda)$), and $> \lambda/6$ for seismometer pairs separated along different directions.

Extending the lower envelope of the scattered points in the left of figure 5 to a coherence value $\Re(\gamma) = 0.5$, we find for day 154 that the minimal distance with $\Re(\gamma) = 0.5$ is about 7 km, and about 3 km for day 191. Assuming isotropy, we can infer for day 154 a seismic speed of about $4 \cdot 0.2 \text{ Hz} \cdot 7 \text{ km} = 5.6 \text{ km/s}$, or 8.4 km/s assuming maximal directional dependence. The corresponding values for day 191 are 2.4 km/s and 3.6 km/s. While the speed values of day 191 are consistent with expected fundamental Rayleigh-wave speeds, the inferred speeds of day 154 are too high.

These observations imply that during day 154, the dominant contribution to the seismic

field comes from body waves, while Rayleigh waves dominate on day 191. The top panel of figure 6 shows a one-year time series of the PSD at 0.2 Hz together with the minimal coherence observed between all seismometer pairs closer than 3 km to each other. The inset plot zooms onto the first 60 days. The expected coherence from an isotropic fundamental Rayleigh-wave field with a speed value of 3.5 km/s (among all plane-wave models, the isotropic model has the highest minimal coherence value) between two seismometers at 3 km distance to each other is 0.73 (assuming negligible instrumental noise). Coherence exceeds this value significantly during many days, and interestingly, a significant decline of coherence is always accompanied with a significant increase of the microseismic amplitude.

This strongly points towards the following model of oceanic microseisms at Homestake. When the oceanic microseisms are weak, i.e., approaching the global low-noise model, then the field is dominated by body waves. Typically week-long, strong transients of Rayleigh waves add to this background of body waves decreasing RPCC values. The existence of body waves in oceanic microseisms is well known and modeled [50, 51]. However, the hypothesis that body waves define the microseismic spectrum at quiet times has not been formulated before to our knowledge. This link seems to exist at the Homestake site at least, and it would be very interesting to obtain direct confirmation using methods from [50].

Understanding the wave content of oceanic microseisms is of high priority for sub-Hz GW detectors where seismic fields produce NN about 1000 times stronger than the instrumental noise required to detect GWs [52–54]. The assumption so far has been that the seismic field is dominated by Rayleigh waves, which greatly helps with the cancellation of the associated NN [55]. Given that NN cancellation in the presence of multiple wave polarizations is a complicated task even for modest cancellation goals [23], continuous body-wave content as observed at Homestake would be a substantial additional challenge for plans to suppress seismic NN at sub-Hz frequencies by large factors.

IV. WIENER FILTERING

In the following analysis, we will use a seismometer at the center of the array to imitate a gravitational-wave test mass. In the case of feed-forward subtraction in gravitational-wave interferometers, a seismic array surrounding the test mass is used to create a Wiener filter [17, 29]. The filters are computed as follows. For samples $y(t_i)$ from a single target

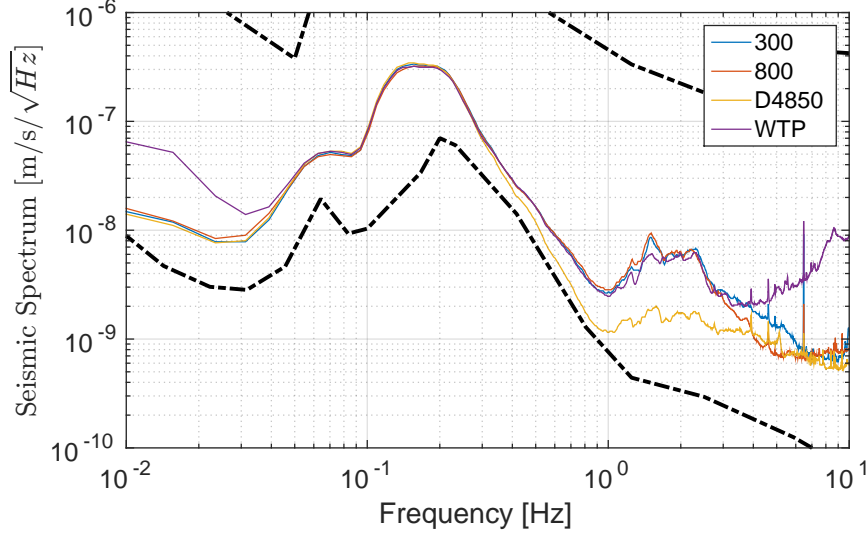


FIG. 7: The median PSD of the vertical channel of the seismometers in the array. These are computed using 128 s segments. Both the primary and secondary microseismic peaks are visible in the data below 1 Hz, while the local anthropogenic sources create significant differences in the spectra above 1 Hz.

channel, M input time series $\vec{x}(t_i) = (x_m(t_i))$ with $m = 1, \dots, M$, and a Wiener filter $\vec{h}(i) = (h_m(i)), i = 0, \dots, N$ that minimizes the residual error, the residual seismic time-series can be written symbolically as a convolution (symbol $*$) [30]:

$$r(t_i) = y(t_i) - \sum_{m=1}^M (h_m * x_m)(t_i), \quad (3)$$

where the convolution is defined as

$$h_m * x_m(t_i) = \sum_{k=0}^N h_m(k) x_m(t_{i-k}), \quad (4)$$

where N is the order of the finite impulse-response filter h .

It is useful to compare the measured residuals to expected estimates. These can be computed as follows. If we denote C_{SS} as the matrix containing the cross spectral densities of witness seismometers, \vec{C}_{ST} as the vector containing the cross spectral densities between the witness and target sensors, and \vec{C}_{TT} as the PSD of the target seismometer, then the average relative noise residual R achieved is given by

$$R(f) = 1 - \frac{\vec{C}_{ST}^\top(f) \cdot C_{SS}^{-1}(f) \cdot \vec{C}_{ST}(f)}{C_{TT}(f)}. \quad (5)$$

When using just a single witness seismometer, this simply reduces to

$$R(f) = 1 - |\gamma(f)|^2 \quad (6)$$

where $\gamma(f)$ is the witness-target coherence as defined in equation (1).

Figure 7 shows the median PSD of seismometer data from vertical channels for a sample of seismometers in this analysis. Occasional strong disturbances like earthquakes contribute negligibly to the median spectrum. The primary and secondary microseismic peaks, occurring between 30 – 100 mHz and 0.1 – 0.5 Hz respectively, are visible with approximately the same amplitude both at the surface and below ground. For surface and near surface stations (e.g., at 300 ft), wind can also be a significant source of low-frequency ground motion, while the effect is insignificant well-below ground [25]. The local anthropogenic sources create significant differences in the spectra above 1 Hz. The stations at depth have a world-class low-noise environment [25, 27].

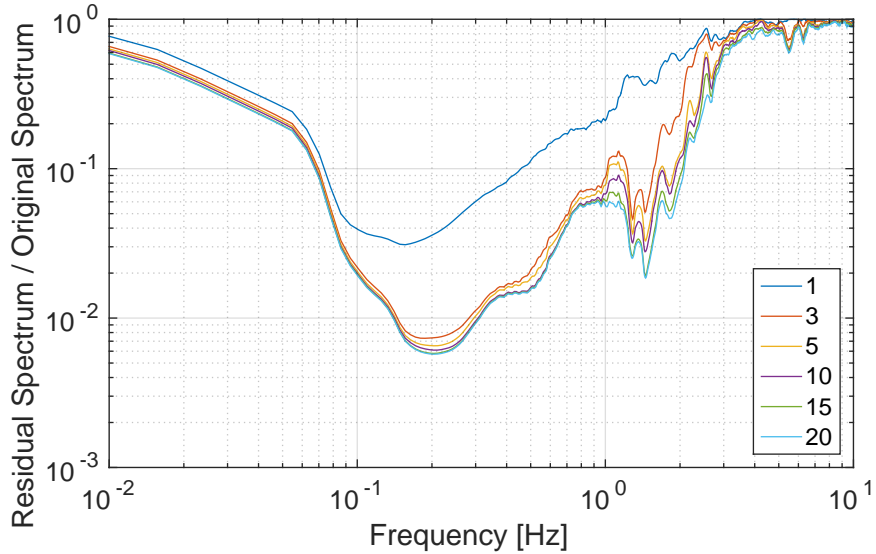


FIG. 8: Expected amplitude residuals, i.e., plotting the square-root of equation (5), for a variety of numbers M of input sensors taken from the Homestake array. The residuals rapidly converge after just a handful of sensors.

In figure 8, we use equation (5) to determine the expected residuals for a few optimal subsets of seismometers taken from the total array. Optimal subsets are the ones that, given a number of seismometers, produce lowest subtraction residuals.

In figure 9, we demonstrate the performance of the filter on the seismic array data using as targets the vertical channels of three seismometers on the 800 ft level, the 4850 ft level, and the surface. We achieve more than a factor of 100 reduction in noise in this band using all available channels. Using only surface stations as witness channels is worse than the configuration where all channels are used by a factor of ≈ 4 . Generally, there is no clearly visible residual microseismic peak except for the case of using surface seismometers as input channels to cancel noise in a 4850 ft seismometer (upper, right plot in figure 9). So we were able to improve over previous results reported in [26], almost reaching the limit set by the sensor noise of the Kinemetrics STS-2 broadband seismometers up to 1 Hz used at the 800 ft station [56].

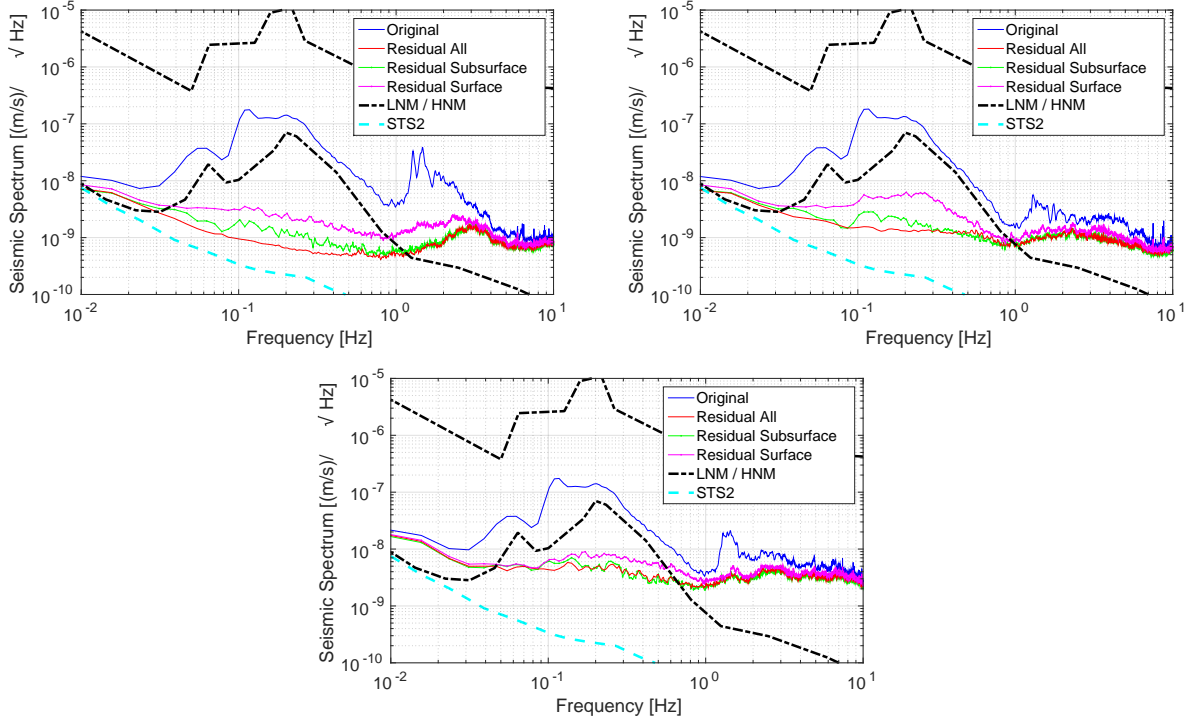


FIG. 9: The plot on the upper left is the subtraction achieved using the seismometer on the 800 ft level as the target channel, up to 10 Hz. The upper right and the bottom plots are the same for the seismometers on the 4850 ft level and the surface, respectively. In each plot, it is shown how the subtraction varies depending on what set of seismometers are used as witness sensors (subsurface, surface, and all). The residual noise can be compared with the STS-2 sensor noise.

On the left of figure 10, we demonstrate the performance of the filter with the 800 ft seismometer as target over a few timescales. We show that a Wiener filter calculated at the

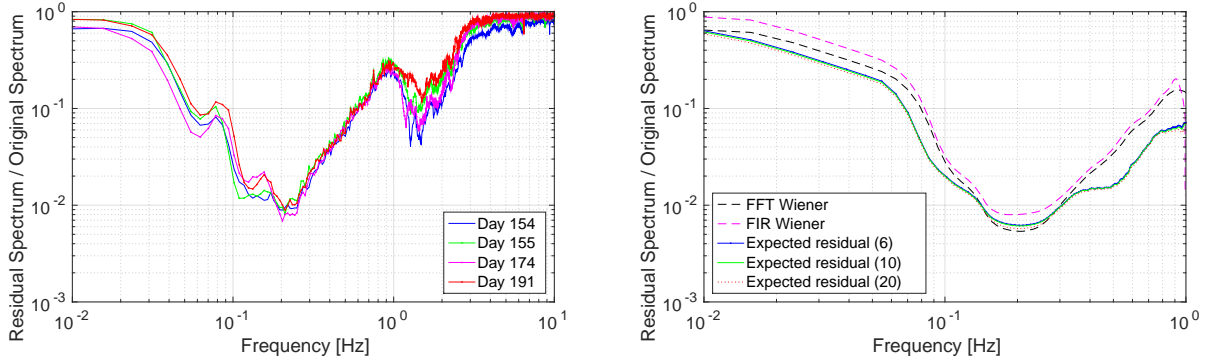


FIG. 10: On the left, we show the performance of the Wiener filter over a few timescales using the vertical channel of the 800 ft station seismometer as the target. This result shows that Wiener filters are efficient in this band over long timescales. On the right, we show the expected residuals given the expression in equation (5) for a number of seismometer arrays and comparisons to both FFT Wiener and FIR Wiener filters for the vertical channel of the 800 ft station.

beginning is efficient over at least month-long timescales. We can evaluate the performance of the filter by comparing the resulting subtraction with the expected residuals given the expression in equation (5) for a number of seismometer arrays. We see on the right of figure 10 that the achieved subtraction is in line with the expected residuals, indicating the efficacy of our implementation. In this plot, we show noise residuals for two different implementations of Wiener filters. One is the frequency-domain filter. The other is the finite-impulse response (FIR) filter applied as shown in equations (3) and (4). The frequency-domain filter typically achieves slightly better cancellation performance since noise in neighboring frequency bins is only weakly correlated, and this correlation can be ignored simplifying the filter. The FIR filter, which is applied in time domain, has to cope with strong correlations potentially between all samples of the time series. This makes it numerically more challenging to calculate the Wiener filter mostly due to large, degenerate correlation matrices, which need to be inverted. In our case, differences between the performances of these two implementations are minor.

V. CONCLUSION

In this paper, we have used one year of data from an underground and surface array deployed in 2015 at the Sanford Underground Research Facility (former Homestake mine)

for correlation analyses of the ambient seismic field. The results include the estimation of Rayleigh-wave speeds between 0.3 Hz and 3.5 Hz, the year-long evolution of spectral density and seismometer correlations at 0.2 Hz, and the broadband cancellation of seismic signals in the array using Wiener filters.

Estimates of seismic speeds were presented as a histogram, which traces a dispersion curve consistent with Rayleigh-wave speeds. Between 1 Hz and 2 Hz, Rayleigh-wave speed is found to be about 2.6 km/s falling to lower values above 2 Hz. Speed estimates below 1 Hz were less accurate limited by the dimension of the array, and above 2.5 Hz because of loss of coherence between seismometers.

The long-term study of PSDs and correlations at 0.2 Hz showed evidence of an incessant background of body waves frequently perturbed by week-long Rayleigh-wave transients. These findings are consistent with previous observations, but our findings go beyond previous results as the body-wave content seems to enforce the low-noise model at the Homestake site. This link has not been established before to our knowledge.

Finally, Wiener filters were calculated for the cancellation of seismic signals in several target sensors using data from the array as input. The residuals achieved here improve over previous results at Homestake with a smaller array. The spectra of residual noise approach the limit set by the instrumental noise over a broad frequency band between about 10 mHz and 0.5 Hz reducing seismic signals by more than 2 orders of magnitude. These results demonstrate the capability of seismic arrays to extract information about ambient seismic fields efficiently to provide coherent estimates of ground displacement at other points in the fields. Such capabilities are essential to realize cancellation of terrestrial gravity noise in future gravitational-wave detectors.

Acknowledgments

MC was supported by the David and Ellen Lee Postdoctoral Fellowship at the California Institute of Technology. We thank the staff at the Sanford Underground Research Facility and PASSCAL for assistance, particularly the help of Tom Regan, Jaret Heise, Jamey Tollefson, and Bryce Pietzyk. This work was supported by National Science Foundation INSPIRE grant PHY1344265. This paper has been assigned LIGO document number LIGO-P1700422.

Appendix A: Additional results

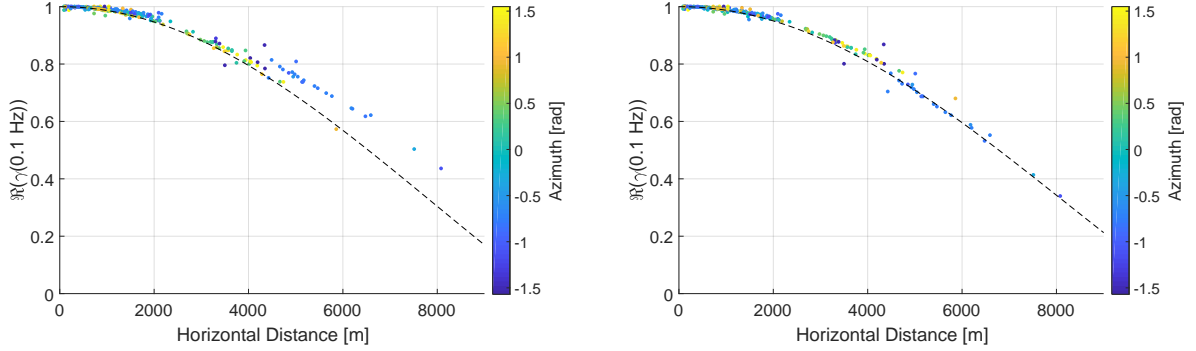


FIG. 11: The RPCC as a function of distance between the vertical channels of all seismometers at 0.1 Hz analogous to figure 5. The isotropic correlation model is shown with speed value 2.7 km/s (left plot), and 2.8 km/s (right plot).

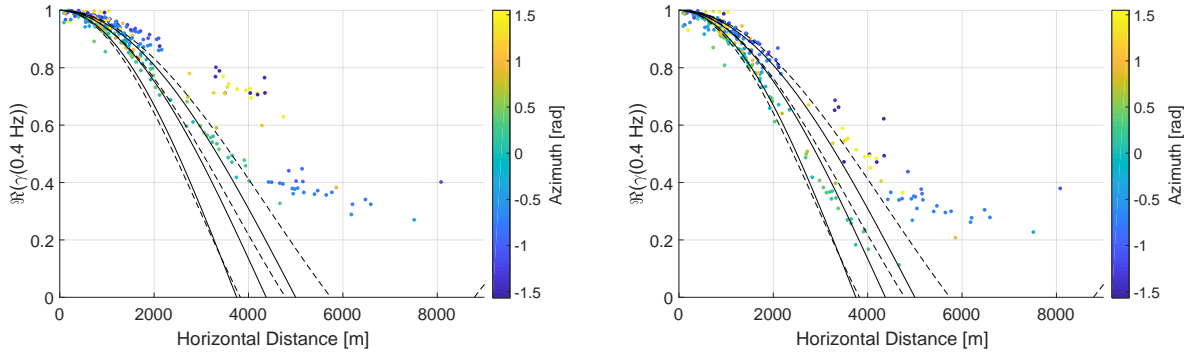


FIG. 12: The RPCC as a function of distance between the vertical channels of all seismometers at 0.4 Hz analogous to figure 5. In both plots, models are shown for the single plane wave (solid lines; speed values 6 km/s, 7 km/s, 8 km/s), and isotropic field (dashed lines; speed values 4 km/s, 5 km/s, 6 km/s).

To check that the anti-correlation between PSDs and minimal coherence at 0.2 Hz is not only present at Homestake, we performed the same analysis for the Sweetwater array [49]. The seismometers in this analysis are from an array in Sweetwater, Texas, which is located at 32°28'5" N and 100°24'26" W. The array consists of two approximate circles, one with about a 10 km diameter, another with a 25 km diameter, with 23 stations with good data quality during March and April 2014. This array has significantly larger horizontal spacing

than the Homestake array, with horizontal distances between the center of the array and other seismometers ranging between 2-14 km. It also has significant variation in elevation over the array, with a max elevation change between seismometers of about 250 m. We perform the same analysis with this array as in the Homestake case, computing the PSDs and coherences between the station pairs. Figure 13 shows $\Re(\gamma)$ vs. the PSDs for the Homestake and Sweetwater arrays. The difference in $\Re(\gamma)$ arises from the different sizes of the arrays.

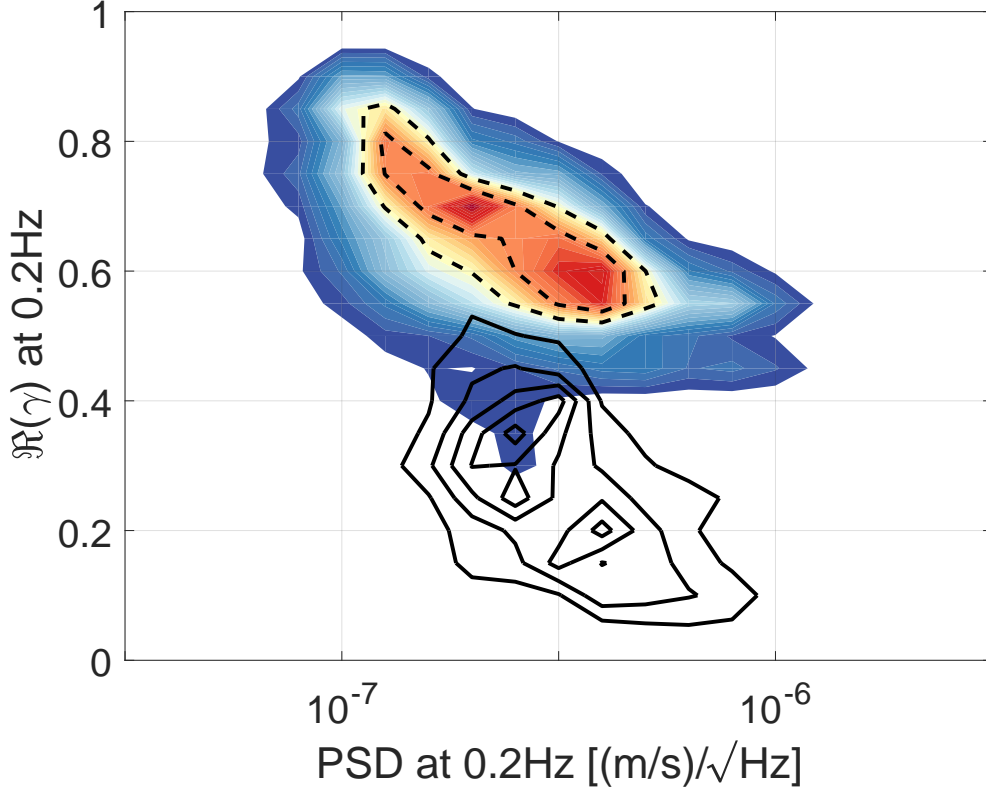


FIG. 13: The plot shows the data in figure 6 as a density plot for the Homestake array (colored contours with contour lines at 0.5 and 0.7) as well as the Sweetwater array (only contour lines at 0.1, 0.3, 0.5, 0.7, and 0.9.).

References

- [1] Abbott, B P et al (LIGO Scientific Collaboration and Virgo Collaboration) 2016 *Phys. Rev. Lett.* **116**(6) 061102 URL <http://link.aps.org/doi/10.1103/PhysRevLett.116.061102>
- [2] Abbott, B P et al (LIGO Scientific Collaboration and Virgo Collaboration) 2016 *Phys. Rev. Lett.* **116**(24) 241103 URL <http://link.aps.org/doi/10.1103/PhysRevLett.116.241103>
- [3] Abbott, B P et al (LIGO Scientific and Virgo Collaboration) 2017 *Phys. Rev. Lett.* **118**(22) 221101 URL <https://link.aps.org/doi/10.1103/PhysRevLett.118.221101>
- [4] Abbott, B P et al (LIGO Scientific Collaboration and Virgo Collaboration) 2017 *Phys. Rev. Lett.* **119**(14) 141101 URL <https://link.aps.org/doi/10.1103/PhysRevLett.119.141101>
- [5] Abbott, B P et al (LIGO Scientific Collaboration and Virgo Collaboration) 2017 *Phys. Rev. Lett.* **119**(16) 161101 URL <https://link.aps.org/doi/10.1103/PhysRevLett.119.161101>
- [6] The LIGO Scientific Collaboration, Aasi J, Abbott B P *et al.* 2015 *Classical and Quantum Gravity* **32** 074001 URL <http://stacks.iop.org/0264-9381/32/i=7/a=074001>
- [7] Acernese F, Agathos M, Agatsuma K *et al.* 2015 *Classical and Quantum Gravity* **32** 024001 URL <http://stacks.iop.org/0264-9381/32/i=2/a=024001>
- [8] Lück H, Affeldt C, Degallaix J *et al.* 2010 *Journal of Physics: Conference Series* **228** 012012 URL <http://stacks.iop.org/1742-6596/228/i=1/a=012012>
- [9] Aso Y, Michimura Y, Somiya K *et al.* (The KAGRA Collaboration) 2013 *Phys. Rev. D* **88**(4) 043007 URL <http://link.aps.org/doi/10.1103/PhysRevD.88.043007>
- [10] Unnikrishnan C S 2013 *International Journal of Modern Physics D* **22** 1341010
- [11] B P Abbott et al 2017 *Classical and Quantum Gravity* **34** 044001 URL <http://stacks.iop.org/0264-9381/34/i=4/a=044001>
- [12] Punturo M, Abernathy M, Acernese F *et al.* 2010 *Classical and Quantum Gravity* **27** 194002 URL <http://stacks.iop.org/0264-9381/27/i=19/a=194002>
- [13] Matichard F, Lantz B, Mason K *et al.* 2014 *Precision Engineering* – ISSN 0141-6359 URL <http://www.sciencedirect.com/science/article/pii/S0141635914001561>
- [14] Matichard F, Lantz B, Mason K *et al.* 2015 *Precision Engineering* **40** 287 – 297 ISSN 0141-6359 URL <http://www.sciencedirect.com/science/article/pii/S0141635914002098>

- [15] Braccini S, Barsotti L, Bradaschia C *et al.* 2005 *Astroparticle Physics* **23** 557 – 565 ISSN 0927-6505 URL <http://www.sciencedirect.com/science/article/pii/S092765050500068X>
- [16] Giaime J A, Daw E J, Weitz M *et al.* 2003 *Review of Scientific Instruments* **74** 218–224 URL <http://scitation.aip.org/content/aip/journal/rsi/74/1/10.1063/1.1524717>
- [17] Driggers J, Evans M, Pepper K and Adhikari R 2012 *Review of Scientific Instruments* **83** 024501–024501
- [18] DeRosa R, Driggers J C, Atkinson D *et al.* 2012 *Classical and Quantum Gravity* **29** 215008 URL <http://stacks.iop.org/0264-9381/29/i=21/a=215008>
- [19] Kokeyama K, Izumi K, Korth W Z *et al.* 2014 *J. Opt. Soc. Am. A* **31** 81–88 URL <http://josaa.osa.org/abstract.cfm?URI=josaa-31-1-81>
- [20] Saulson P R 1984 *Phys. Rev. D* **30** 732
- [21] Hughes S A and Thorne K S 1998 *Phys. Rev. D* **58** 122002
- [22] Creighton T 2008 *Class. Quantum Grav.* **25** 125011
- [23] Harms J 2015 *Living Reviews in Relativity* **18** URL <http://www.livingreviews.org/lrr-2015-3>
- [24] Beker M, Cella G, DeSalvo R *et al.* 2011 *General Relativity and Gravitation* **43** 623–656
- [25] Harms J, Acernese F, Barone F *et al.* 2010 *Classical and Quantum Gravity* **27** 225011
- [26] M Coughlin J Harms e a 2014 *Classical and Quantum Gravity* **31** 215003
- [27] Mandic V, Tsai V C, Pavlis G L *et al.* 2017 *Submitted to Seismological Research Letters*
- [28] Cella G 2000 Off-line Subtraction of Seismic Newtonian Noise *Recent Developments in General Relativity* (Springer) pp 495–503
- [29] Driggers J C, Harms J and Adhikari R X 2012 *Phys. Rev. D* **86**(10) 102001 URL <http://link.aps.org/doi/10.1103/PhysRevD.86.102001>
- [30] Vaseghi S V 2001 *Wiener Filters* (John Wiley & Sons, Ltd) pp 178–204 ISBN 9780470841624
- [31] Sayed A H 2003 *Fundamentals of Adaptive Filtering* (John Wiley & Sons)
- [32] Coughlin M and Harms J 2012 *Classical and Quantum Gravity* **29** 075004 URL <http://stacks.iop.org/0264-9381/29/i=7/a=075004>
- [33] Longuet-Higgins M S
- [34] Gerstoft P and Tanimoto T 2007 *Geophysical Research Letters* **34** L20304
- [35] Kedar S, Longuet-Higgins M, Webb F *et al.* 2008 *Proceedings of the Royal Society of London A: Mathematical, Physical and Engineering Sciences* **464** 777–793 ISSN 1364-5021

- (*Preprint* <http://rspa.royalsocietypublishing.org/content/464/2091/777.full.pdf>) URL <http://rspa.royalsocietypublishing.org/content/464/2091/777>
- [36] Ardhuin F, Stutzmann E, Schimmel M and Mangeney A 2011 *Journal of Geophysical Research: Oceans* **116** n/a–n/a ISSN 2156-2202 c09004 URL <http://dx.doi.org/10.1029/2011JC006952>
 - [37] Ermert L, Villaseñor A and Fichtner A 2016 *Geophysical Journal International* **204** 347–364 ISSN 1365246X
 - [38] Gerstoft P, Shearer P M, Harmon N and Zhang J 2008 *Geophysical Research Letters* **35** n/a–n/a ISSN 1944-8007 l23306 URL <http://dx.doi.org/10.1029/2008GL036111>
 - [39] Capon J 1969 *Proceedings of the IEEE* **57** 1408–1418 ISSN 0018-9219
 - [40] Rost S and Thomas C 2002 *Reviews of Geophysics* **40** ISSN 8755-1209 URL <http://www.agu.org/pubs/crossref/2002/2000RG000100.shtml>
 - [41] Harmon N, Gerstoft P, Rychert C A *et al.* 2008 *Geophysical Research Letters* **35** n/a URL <GotoISI>://WOS:000259803200006
 - [42] Gal M, Reading A, Ellingsen S *et al.* 2014 *Geophysical Journal International* **198** 1045–1054 ISSN 0956-540X
 - [43] Tsai V C 2011 *Journal of Geophysical Research* **116** B09311 ISSN 0148-0227 URL <http://doi.wiley.com/10.1029/2011JB008483>
 - [44] Yang Y, Ritzwoller M H, Levshin A L and Shapiro N M 2007 *Geophysical Journal International* **168** 259–274
 - [45] Bensen G D, Ritzwoller M H, Barmin M P *et al.* 2007 *Geophysical Journal International* **169** 1239–1260
 - [46] Prieto G A, Lawrence J F and Beroza G C 2009 *Journal of Geophysical Research: Solid Earth* **114** n/a–n/a ISSN 2156-2202 b07303 URL <http://dx.doi.org/10.1029/2008JB006067>
 - [47] Lawrence J F and Prieto G A 2011 *Journal of Geophysical Research: Solid Earth* **116** n/a–n/a ISSN 2156-2202 b06302 URL <http://dx.doi.org/10.1029/2010JB007836>
 - [48] Foster A, Ekström G and Nettles M 2014 *Geophysical Journal International* **196** 1189–1206 URL [+http://dx.doi.org/10.1093/gji/ggt454](http://dx.doi.org/10.1093/gji/ggt454)
 - [49] Barklage M, Hollis D, Gridley J M, Woodward R and Spriggs N 2014 *AGU Fall Meeting Abstracts*
 - [50] Landès M, Hubans F, Shapiro N M, Paul A and Campillo M 2010 *Journal of Geophysical*

Research: Solid Earth **115** n/a–n/a ISSN 2156-2202 b05302 URL <http://dx.doi.org/10.1029/2009JB006918>

- [51] Obrebski M, Arduin F, Stutzmann E and Schimmel M 2013 *Journal of Geophysical Research: Solid Earth* **118** 4312–4324 ISSN 2169-9356 URL <http://dx.doi.org/10.1002/jgrb.50233>
- [52] Paik H J, Griggs C E, Moody M V *et al.* 2016 *Classical and Quantum Gravity* **33** 075003 URL <http://stacks.iop.org/0264-9381/33/i=7/a=075003>
- [53] McManus D J, Forsyth P W F, Yap M J *et al.* 2017 *Classical and Quantum Gravity* **34** 135002 URL <http://stacks.iop.org/0264-9381/34/i=13/a=135002>
- [54] Shoda A, Ando M, Ishidoshiro K *et al.* 2014 *Phys. Rev. D* **89**(2) 027101 URL <http://link.aps.org/doi/10.1103/PhysRevD.89.027101>
- [55] Harms J and Paik H J 2015 *Phys. Rev. D* **92**(2) 022001 URL <http://link.aps.org/doi/10.1103/PhysRevD.92.022001>
- [56] STS-2 were used everywhere in the array except for stations DEAD, ROSS, YATES, 300, where Gralp 3T were deployed